Static and dynamic compressive behaviour of 3D printed auxetic lattice reinforced ultra-high performance concrete

Meng Chen[a,b], Zegang Chen[a], Yiwei Xuan[c], Tong Zhang[a], Mingzhong Zhang[c,*]

[a] *School of Resources and Civil Engineering, Northeastern University, Shenyang, 110819, China*

[b] *Institute for Frontier Technologies of Low-Carbon Steelmaking, Northeastern University, Shenyang, 110819, China*

[c] *Department of Civil, Environmental and Geomatic Engineering, University College London, London, WC1E 6BT, UK*

Abstract: This paper presents a systematic experimental study on static and dynamic compressive behaviour of 3D octet, re-entrant honeycomb and triangular lattice reinforced ultra-high performance concrete, i.e., O-UHPC, H-UHPC and T-UHPC as well as steel fibre reinforced UHPC (S-UHPC). Mechanical tests were conducted to investigate the static and dynamic compressive behaviour of UHPC composites including failure pattern, stress-strain curve, dynamic increase factor (DIF), dynamic compressive strain and energy dissipation under various strain rates (i.e., 0, 34.8, 59.7, 86.7, 108.5 and 134.7 s^{-1}). The plain UHPC and S-UHPC were used as references for comparison. Results indicate that H-UHPC has a 14.6-19.4% higher static compressive strength than O-UHPC and T-UHPC. S-UHPC exhibits higher dynamic compressive strength at lower strain rates, while the dynamic strengths of H-UHPC and T-UHPC at higher strain rates reach the highest, i.e., 262.7 MPa and 222.2 MPa, respectively. The highest total energy and post-crack energy at high strain rates take place on H-UHPC. Overall, H-UHPC has comparable static compressive behaviour but better dynamic compressive behaviour at high strain rates in terms of strength, ductility, energy dissipation and DIF, compared with other UHPC specimens, suggesting that re-entrant honeycomb is a better choice for manufacturing UHPC with optimal auxetic 3D lattices.

Keywords: Ultra-high performance concrete; Metamaterials; Auxetic lattice; 3D printing; Dynamic properties; Split Hopkinson pressure bar

1. Introduction

Auxetics are innovative and advanced mechanical structural materials with negative Poisson's ratio (NPR), which shrink horizontally when subjected to uniaxial compression and expand horizontally under tension. Compared with conventional materials, auxetic materials, also called metamaterials, exhibit higher shear modulus [1, 2], excellent indentation resistance [3-5], energy absorption capacity [6-9] , fracture toughness [10], viscoelastic properties [11], synclastic properties [12], variable permeability [13], and resistance to pull-out and delamination, which have been increasingly used for different applications such as medical collapsible brackets [14, 15], energy-absorbing protective

* Corresponding author. Email address: mingzhong.zhang@ucl.ac.uk (M. Zhang)

devices [16-20], industrial fasteners [21], smart sensors [22, 23], textile industry [24, 25], adjustable resistance tape for seismic waves [26, 27]. Based on microscopic structural geometry and corresponding deformation mechanisms, auxetic structures can be classified into re-entrant structures [28-31], rotating unit structures [32-35], chiral structures [36-38], perforated sheets structures [39], nodule fibril structures [40-42], buckling induced structures [43, 44] and hybrid structures [45-47]. As one of the most common auxetic structure, re-entrant structures formed by truss presents bi-directional NPR, high porosity and superior mechanical properties with optimised geometry [48, 49].

Generally, the auxeticity of most auxetic structures is derived from the deformation of lattice structures with high porosity that provides a prospect of incorporating filler materials into auxetic lattice [50]. A growing number of studies focus on the mechanical properties of auxetic lattice reinforced composites, among which the auxetic lattice acts as reinforcement while the filler phase is matrix. The investigation on static compressive behaviour of auxetic Warmuth and Hexaround lattice reinforced composites indicates that filling VeroWhite and TangoBlack+ results in higher stress, delayed densification and up to 316% and 40% rise in elastic modulus for Warmuth and Hexaround composite, respectively [51]. It was also reported that the typical chiral lattice reinforced composites filled with foam exhibit higher stiffness and 106.6% higher specific energy absorption compared to the equivalent void lattice [52]. Under dynamic compression, around 40-70% higher plateau stress can be found for 3D re-entrant, 2D re-entrant and 2D missing rib lattice reinforced composites against equivalent lattice [53]. The composites could bear multi-axial compression due to the NPR effects of auxetic frame in compression, bringing a synergistic effect between the filler and auxetic reinforcement [16, 52]. The transverse deformation of fillers is restricted by auxetic lattice, while the friction between lattice and matrix enhances the difficulty of struts sliding [54, 55]. However, as a trade-off between NPR effects and stiffness, auxetic lattice reinforced composites tend to have a weaker auxeticity relative to the correspondent lattice [50, 56]. The geometry of auxetic lattice holds a significant influence on the overall mechanical behaviour of the composites. Re-entrant lattice reinforced composite filled with soft material exhibits nearly four times higher elastic modulus and three times higher energy absorption than the equivalent chiral and two non-auxetic composites [16]. It was found that the average plateau stress of 2D re-entrant reinforced composites filled with strain rate sensitive material under quasi-static compression was 79-85 MPa that was about 155% and 182% respectively higher than that of the equivalent 3D re-entrant and 2D missing rib composite. The dynamic average plateau stress of 2D re-entrant, 3D re-entrant and 2D missing rib lattice reinforced composites also was in the range of 121-123 MPa, 56-72 MPa and 52-57 MPa, respectively, presenting similar trends, while 2D re-entrant lattice has much better mechanical response during compression [53]. In recent years, apart from typical uniform auxetic lattice reinforced composites, the graded auxetic lattice reinforced composites were also explored, the specific energy absorption of

which at up to 60% and 80% deformation was found to be around 61.2% and 65.2% lower than that of the corresponding uniform chiral lattice reinforced composite [57].

The filling materials play an important role in the overall mechanical properties of auxetic lattice reinforced composites [50]. Most of existing studies adopted foam and rubber materials as fillers to achieve better compressive performance [5, 16, 51, 58], while the mechanical behaviour of auxetic lattice filled with cementitious materials is rarely explored. The experimental study on quasi-static compressive behaviour of aluminium based uniform and layered re-entrant lattice filled with normal concrete indicated that although both composites show X-shape shear failure pattern under compression, the layered configuration enhances the shear resistance, overall stability and specific energy absorption of the composite [59]. Another research on the mechanical properties of 2D typical re-entrant lattice filled with foam concrete under quasi-static and low-velocity compression found that the effective reinforcement of re-entrant lattice avoids premature failures, while the closer interaction between lattice and foam concrete further brings better energy absorption capacity and efficiency in the re-entrant lattice reinforced foam concrete [60]. The strength and relative stiffness of foam concrete and the re-entrant lattice determine the deformation modes, while the failure patterns of the composites under quasi-static compression change gradually from compressive failure to shear failure with the increase of density of foam concrete. The NPR effect of the re-entrant lattice reinforced foam concrete reduces obviously with the rise in density of foam concrete under compression. Similarly, steel 3D re-entrant lattice reinforced mortar was proposed by Tzortzinis et al. [61]. The periodicity in 3D of re-entrant lattice averts weak link failure of the composite compared with conventional confinement and the transverse in deformation behaviour and loading condition of struts derived from auxeticity gradually enhance the confinement ability of the lattice [62]. The auxetic lattice reinforced mortar exhibits a 140% higher compressive strength and more ductile post-peak behaviour compared to conventional confinement. Different from the aforementioned ordinary cementitious filling materials, ultra-high performance concrete (UHPC) normally made up of Portland cement, supplementary cementitious materials such as fly ash, ground granular blast-furnace slag and silica fume, superplasticiser, and fine aggregates at optimal proportions can achieve superior strength, elastic modulus and other engineering properties as the porosity and other internal defects can be reduced, while the compactness can be significantly improved [60, 63]. UHPC can achieve an even higher ductility and resilience by incorporating steel fibres, whereas leading to a considerable initial cost of UHPC and the disordered fibre distribution could reduce its engineering properties [64]. Similar as steel fibre reinforcement, the incorporation of auxetic lattice reinforcement into a matrix with high stiffness (like UHPC) can help withstand its tensile loading [56] and thus improve its toughness and ductility [65]. A systematic study on the static and dynamic compressive behaviour of auxetic lattice reinforced UHPC is still lacking to date.

The main purpose of this paper is to study the effect of auxetic lattice on mechanical performance of UHPC through a systematic investigation on the static and dynamic compressive behaviour of three types of 3D printed auxetic lattice reinforced UHPC with an almost same volume fraction of 14.1%. First, octet reinforced UHPC (O-UHPC), re-entrant honeycomb reinforced UHPC (H-UHPC) and re-entrant triangular reinforced UHPC (T-UHPC) were designed and prepared, respectively. For comparison, the plain UHPC (P-UHPC) and steel fibre reinforced UHPC (S-UHPC) were used as the reference composites. Afterwards, a series of static and dynamic compressive tests were conducted on the auxetic lattice reinforced composites at various impact strain rates (i.e., 0, 34.8, 59.7, 86.7, 108.5 and 134.7 s^{-1}). Based on the obtained experimental results, the effects of different types of auxetic reinforcement and strain rates on the dynamic compressive behaviour of UHPC were explored and the underlying mechanisms were discussed in detail.

2. Experimental program

2.1 Materials

2.1.1 Polylactic acid (PLA) lattice

Polylactic acid (PLA), one of the most widely used polymeric filament material for 3D printing, was adopted to produce auxetic lattices. Compared to acrylonitrile butadiene styrene (ABS) that is another most used 3D printing material, no additional support is required for PLA during the printing process of octet lattice [65, 66]. Thus, PLA is more suitable for manufacturing auxetic lattice reinforcement for concrete. The physical and mechanical properties of PLA polymeric filaments including density, elastic modulus, tensile strength and percentage of breaking elongation are shown in Table 1.

Table 1 Properties of PLA polymeric filaments used for auxetic lattices.

Density (g/cm^3)	Elastic modulus (GPa)	Tensile strength (MPa)	Percentage of breaking elongation (%)
1.25	3	60	3

2.1.2 Ultra-high performance concrete (UHPC) filler

Table 2 presents the mix proportion of UHPC as filler employed in this study, where the main binder was Portland cement (P.O 52.5) with density of 3000 kg/m^3. Silica fume with an average particle size of 0.1-0.15 μm and specific surface area of 15-27 m^2/g was used as the active powder to improve the pore structure and mechanical properties of UHPC. High-quality silica sand with a maximum particle size smaller than 450 μm was adopted as fine aggregate. To enhance the flowability of fresh mixtures, polycarboxylate-based superplasticisers (SPs) with a fixed content of 0.5% by mass of the total binder were added during the mixing process for all UHPC specimens [67].

For comparison, steel fibre reinforced UHPC (S-UHPC) was fabricated as the reference composite, where the copper-plated steel fibres with an average length of 13 mm and diameter of 0.2 mm were added at a volume fraction of 2% according to a previous study [68] that such steel fibre content can result in the desirable strength and toughness of UHPC. The density and tensile strength

of steel fibre were 7800kg/m^3 and 2000 MPa, respectively.

Table 2 Mix proportion of ultra-high performance concrete (UHPC) filler (kg/m^3).

Cement	Silica fume	Silica sand	Water	Superplasticizers
788	200	1100	182	21

2.2 Specimen preparation

2.2.1 Auxetic lattice structures

Solidworks software was employed to develop unit cells and 3D models of lattice structures. Three configurations of lattice were designed as reinforcement for UHPC: octet structure, re-entrant honeycomb structure and re-entrant triangular structure, the specific unit structures and 3D models of which are illustrated in Table 3. The volume fraction of lattice reinforcement in UHPC was kept as around 14.1% for them by tailoring the diameter and thickness of lattice struts.

The octet structure ($66.62 \times 66.62 \times 66.62$ mm^3) comprised of $4 \times 4 \times 4$ unit cells. The diameter and length of struts were 1.52 mm and 11.78 mm, respectively, while the distance between the adjacent convex vertices was 16.66 mm. Differently, the total dimension of re-entrant honeycomb structure was $69.69 \times 69.69 \times 68.68$ mm^3, consisting of $4 \times 4 \times 3$ unit cells. The unit cell with vertical strut length of 21.30 mm, inclined strut length of 11.87 mm, re-entrant angle of 45°, and square strut thickness of 2.57 mm was proposed. The re-entrant triangular lattice was designed, with total dimension of $67.88 \times 67.88 \times 67.92$ mm^3 and unit cell numbers of $3 \times 3 \times 6$. The edge length of all corner vertex was set the same as the thickness of strut, i.e., 3.11 mm. The re-entrant angles were 15° and 45°, respectively, while the unit height was 11.31 mm.

The three lattice structures were manufactured by FDM technology using the JGmaker A5S printer (Shenzhen JG Aurora Technology Co., Ltd, China). Table 4 gives the printing parameters. As displayed in Table 3, there is no support on the lower side of re-entrant vertex in the two re-entrant auxetic structures, indicating that it is hard to print the whole lattice structure via FDM directly. Although the difficulty can be solved by incorporating dissolvable supporting materials inside the auxetic structures, the manufacturing cost would be significantly increased. Hence, the interlocking splicing method was used in this study [69], as shown in Fig. 1. The flat components were designed for re-entrant honeycomb and triangular structures and then easily fabricated by conventional fabrication methods including stamping, cutting, casting and FDM. The printed identical components were placed equidistantly in parallel, while different components were orthogonally spliced. The grooves and protrusions were mortised together and reinforced with cyanoacrylate glue to finally form 3D lattices.

Table 3 2D and 3D unit and monolithic structures for three types of lattices (mm).

	Octet	Re-entrant honeycomb	Re-entrant triangular
2D unit	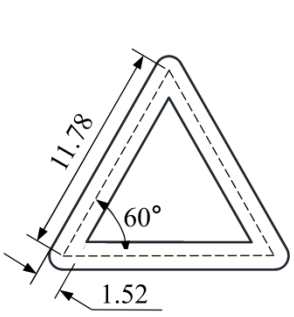	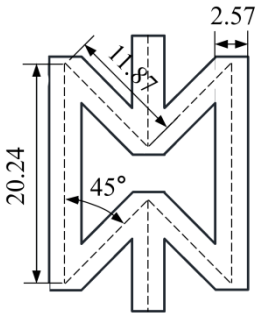	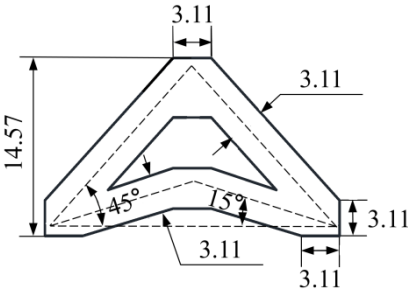
3D unit structure	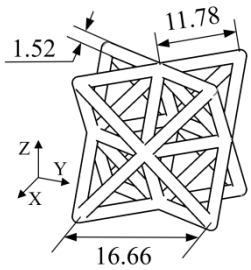	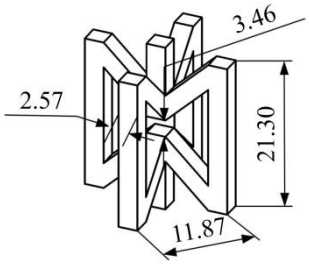	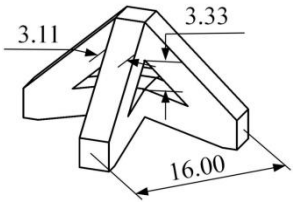
3D lattice	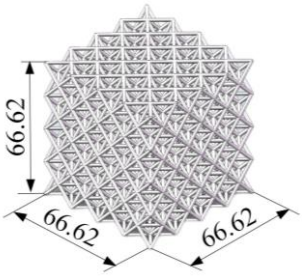	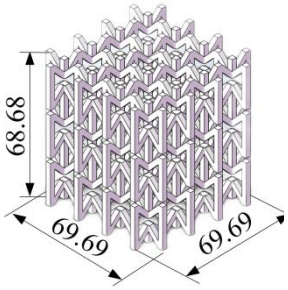	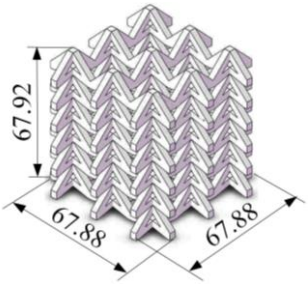

Table 4 Printing parameters for manufacturing auxetic lattices.

Nozzle diameter (mm)	Layer height (mm)	Filling density (%)	Printing speed (mm/s)
0.4	0.15	40	60

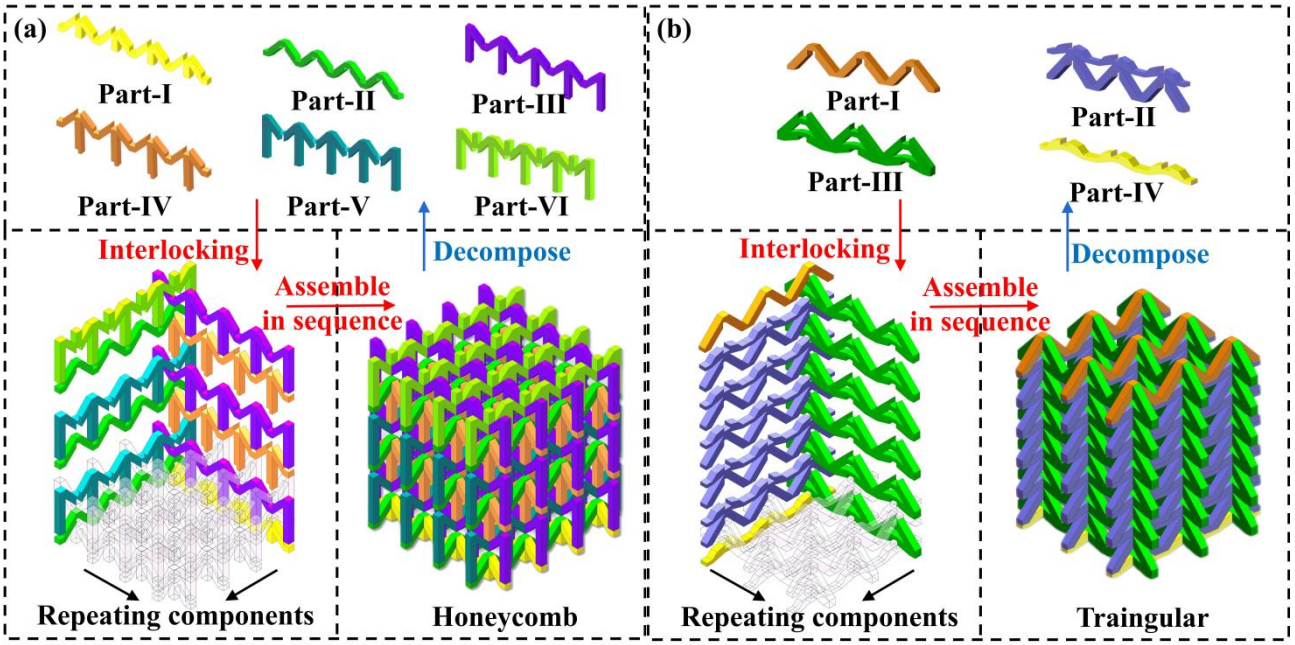

Fig. 1. Flat components, final lattices and assembly methods of (a) re-entrant honeycomb, and (b) re-entrant triangular.

2.2.2 Steel fibre reinforced UHPC (S-UHPC)

Regarding the mixing process of S-UHPC, dry materials including silica sand, silica fume and cement were first dry mixed for 2 min. SPs was then gradually added and mixed thoroughly, followed by the incorporation and uniform distribution of steel fibres for 3 min. Afterwards, water was slowly added and mixed at high-speed for another 2.5 min until the mixture reached the maximum flowability. The fresh mixture was then immediately cast into cube moulds (70.7 × 70.7 × 70.7 mm^3) and vibrated on a vibration table. Finally, all mixtures were cured for 24 h and then de-moulded and stored in a standard curing room (20 ± 2 ℃ and 95% RH) for another 27 d. To prevent errors caused by the specimens not being clamped during the test, the end faces of the cubic specimens should be grinded flat until the non-parallel error between both faces did not exceed 0.1 mm, and the deviation between the end faces and the axis did not exceed 0.25°. The slump test indicated that the slump values of P-UHPC and S-UHPC were 263.5 ± 5.4 mm and 228.8 ± 4.8 mm, respectively.

2.2.3 Auxetic lattice reinforced UHPC

In this study, auxetic lattice reinforced UHPC consists of three categories: octet reinforced UHPC, re-entrant honeycomb reinforced UHPC, and re-entrant triangular reinforced UHPC. A schematic illustration of lattice reinforced UHPC specimen preparation is given in Fig. 2. During the casting process, the fresh UHPC mixture was poured into the cube moulds (70.7 × 70.7 × 70.7 mm^3) with a lattice inside. As shown in Fig. 2, four small plastic pads with size of 3 × 3 × 0.8 mm^3 were placed under the lattice corners to form a protective layer. The injection of concrete for auxetic lattice reinforced UHPC was smoother and more uniform than that for octet reinforced UHPC, which can be ascribed to the longitudinal through geometry of auxetic lattices. The potential internal defects can be significantly reduced, thus improving the overall workability of concrete. The lattice was subjected to a 1 kg additional weight through the air hole of the mould during curing to prevent floating.

For data reliability, three repetitions were set for five specimens of static compressive test. Five reasonable strain rates were employed for five specimens of dynamic compressive test, and three sets of tests were repeated for each strain rate. The number of specimens tested is summarised in Table 5.

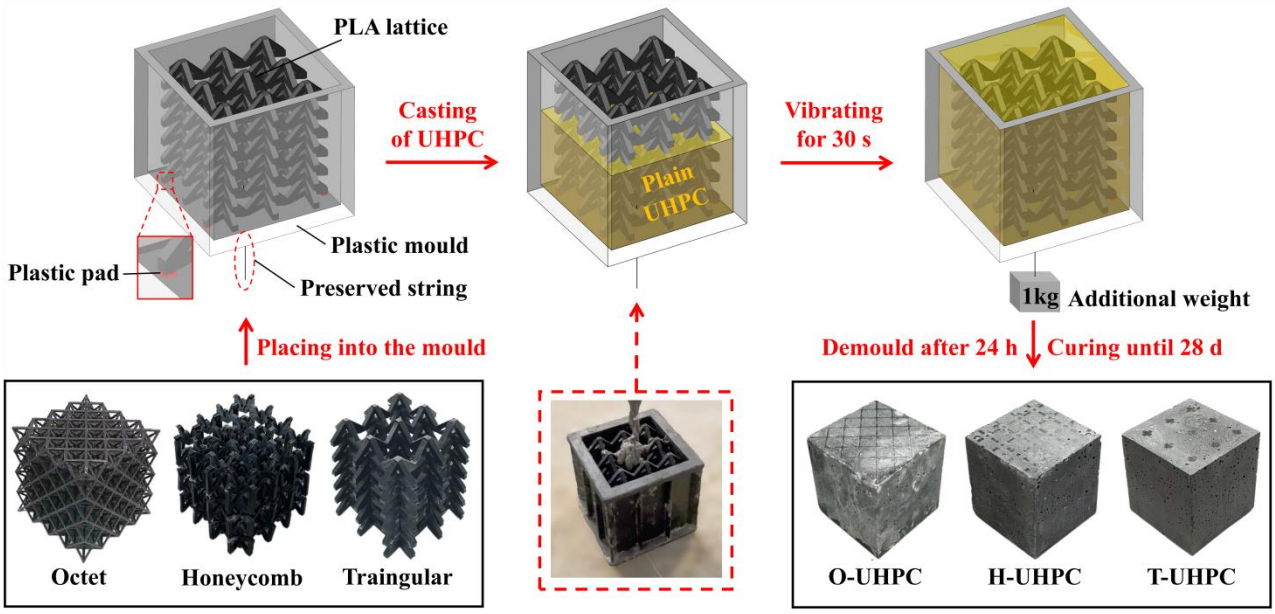

Fig. 2. Schematic illustration of lattice reinforced UHPC specimen preparation.

Table 5 Number of specimens for static and dynamic compressive tests.

Symbol	Static test	Target strain rates in dynamic test (s^{-1})				
		35	60	85	110	135
P-UHPC	3	3	3	3	3	3
S-UHPC	3	3	3	3	3	3
O-UHPC	3	3	3	3	3	3
H-UHPC	3	3	3	3	3	3
T-UHPC	3	3	3	3	3	3

2.3 Test methods

2.3.1 Static compressive test

The static compressive test was performed by a microcomputer-controlled electro-hydraulic servo universal testing machine (1000 kN) with force gauges of 10^{-6} kN accuracy. The loading rate was set as 0.6 MPa/s. The front side of the cubic specimens was sprayed with white pigments to facilitate the observation of crack development. During the compressive process, the cubic specimens was placed to aligned with the centre of pressure plate of the testing machine. Two linear variable displacement transducers (LVDTs) with accuracy of 10^{-5} mm were placed between the upper and lower platforms on the left and right sides of platforms. The average value was taken as the displacement value. A digital camera was placed in the front to record the displacement and damage patterns of the specimens under loading.

2.3.2 Dynamic compressive test

The dynamic compressive test was conducted using SHPB [70, 71], according to a previous study [64]. As illustrated in Fig. 3, the main components consist of a 600 mm striker bar, a 5000 mm incident bar, a 3500 mm transmission bar and a 1200 mm absorbing bar, which were manufactured from high-strength alloy steel. The subsidiary components contain a launching device, a velocity

detecting device, a strain collecting device and an absorber. By adjusting the gas pressure in the nitrogen cylinder and the depth of the striker bar, the impact load was imposed on the specimens at six various velocities of around 4.6, 5.9, 7.8, 8.5 and 11.1 m/s, corresponding to strain rates of around 34.8, 59.7, 86.7, 108.5 and 134.7 s^{-1}, respectively. Three sets of tests were repeated for each velocity. The strain rates of the same specimens show a linear positive correlation with the impact velocities.

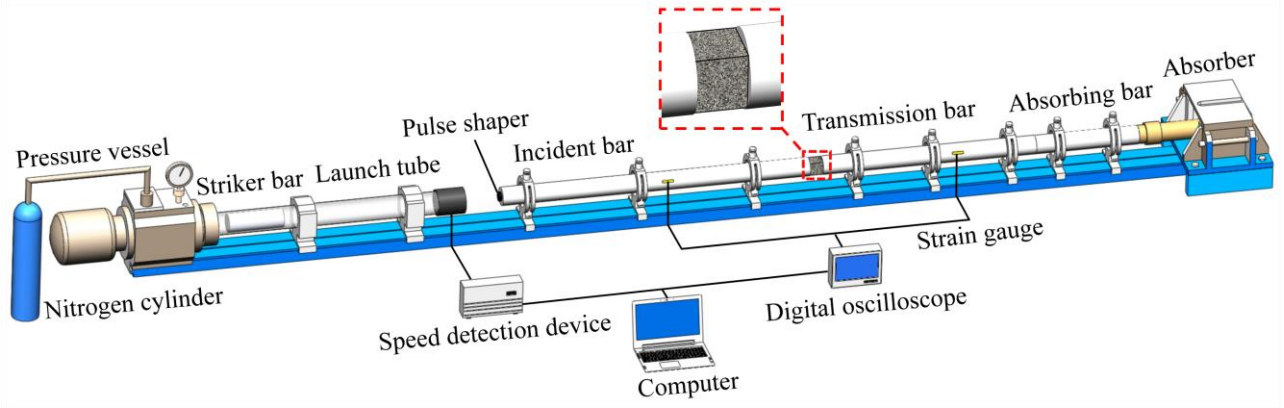

Fig. 3. Splitting Hopkinson pressure bar (SHPB) testing system.

The experimental procedure and principle were the same as that given in a previous study [72]. To guarantee the accuracy of test results, the pulse shaping technique was adopted, which not only attenuated the wave shock to minimise the dispersion and inertia effect in the test [73], but also prolonged the rising time of the incident pulse to ensure the stress equilibrium inside the test specimen [70]. Hence, a rubber pulse shaper of 50 mm in diameter and 2 mm in height was adopted. The smooth sloping waveform using the pulse shaper was displayed in Fig. 4. It is clearly indicated that the combination of the incident wave and reflected waves was approximately equal to the transmitted wave, meaning that a stress balance was achieved.

There are two main assumptions in the theory of elastic stress wave propagation [74]: (1) one-dimensional elasticity wave in the bars; and (2) uniaxial uniform stress and strain in the specimens. The test data were processed using the three-wave method. Stress $\sigma_s(t)$, strain $\varepsilon_s(t)$ and strain rate $\dot{\varepsilon}_s(t)$ were calculated as follows:

$$\begin{cases} \sigma_s(t) = \dfrac{EA_0}{2A_S}\left[\varepsilon_i(t)+\varepsilon_r(t)+\varepsilon_t(t)\right] \\ \varepsilon_s(t) = \dfrac{C_0}{l_S}\displaystyle\int_0^t \left[\varepsilon_i(t)-\varepsilon_r(t)-\varepsilon_t(t)\right]dt \\ \dot{\varepsilon}_s(t) = \dfrac{C_0}{l_S}\left[\varepsilon_i(t)-\varepsilon_r(t)-\varepsilon_t(t)\right] \end{cases} \tag{1}$$

where E is the elastic modulus of the bars (MPa), A_0 represents the cross-sectional area of the bars (mm^2), A_s denotes the cross-sectional area of the specimen (mm^2), C_0 is the longitudinal velocity of the wave (m/s), and l_s stands for the initial thickness of the specimen (mm).

Fig. 5 demonstrates an example of how the final curve for each specimen was derived. Generally, the curves used for the result analysis were obtained by averaging three curves at similar strain rates, while the average strain rate was regarded as the strain rate. Given the brittle and inhomogeneous properties of UHPC and low failure strain at high velocity impact [75, 76], the strain rate would be different for same specimens under the incident velocity. The aforementioned pulse shaping technique could be used to ensure a stress equilibrium for each specimen and a nearly constant strain rate [74-76], which ensures the reliability of the test results.

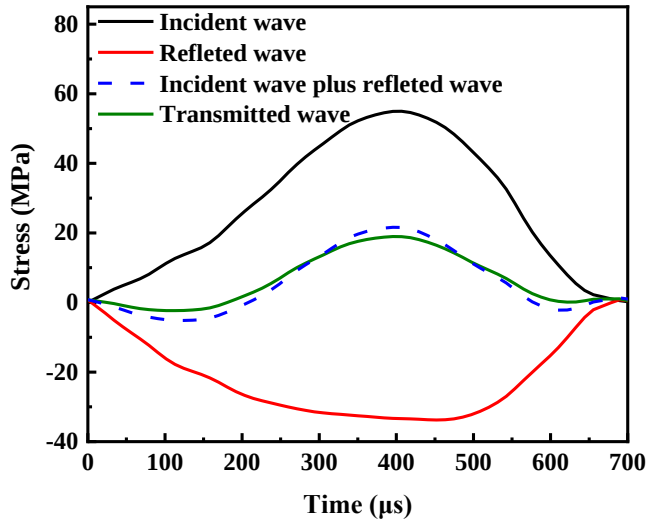

Fig. 4. An example of checking stress equilibrium.

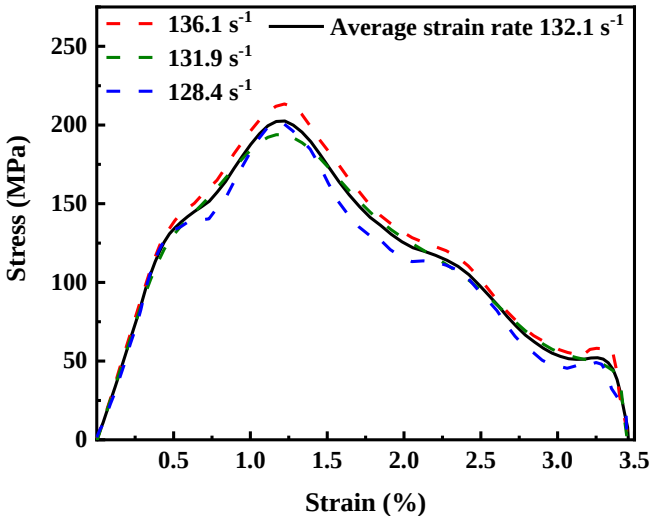

Fig. 5. An example of obtaining dynamic compressive stress-strain curves.

3 Results and discussion

3.1 Static compressive behaviour

3.1.1 Failure patterns

As seen in Fig. 6, UHPC reinforced with different lattices exhibited different failure patterns in compression. The cracks of P-UHPC first generated longitudinally as the load reached 608.0 kN (95.7% P_u). Then, multiple wide longitudinal cracks rapidly appeared and developed, followed by the whole UHPC specimen breaking into fractured pieces. In comparison, the initial crack of S-UHPC was

formed at 699.4 kN (89.7% P_u), which grew as the load increased while the steel fibres tightly bonded to concrete matrix (Fig. 6f). The bridging action of steel fibre across the cracks could effectively delay the generation and reduce the development of micro- and macro-cracks [77, 78]. Afterwards, the inclined and smaller cracks formed and gradually penetrated the specimen. Finally, the S-UPHC specimen failed at the load of 779.8 kN, which is greater than that of P-UHPC.

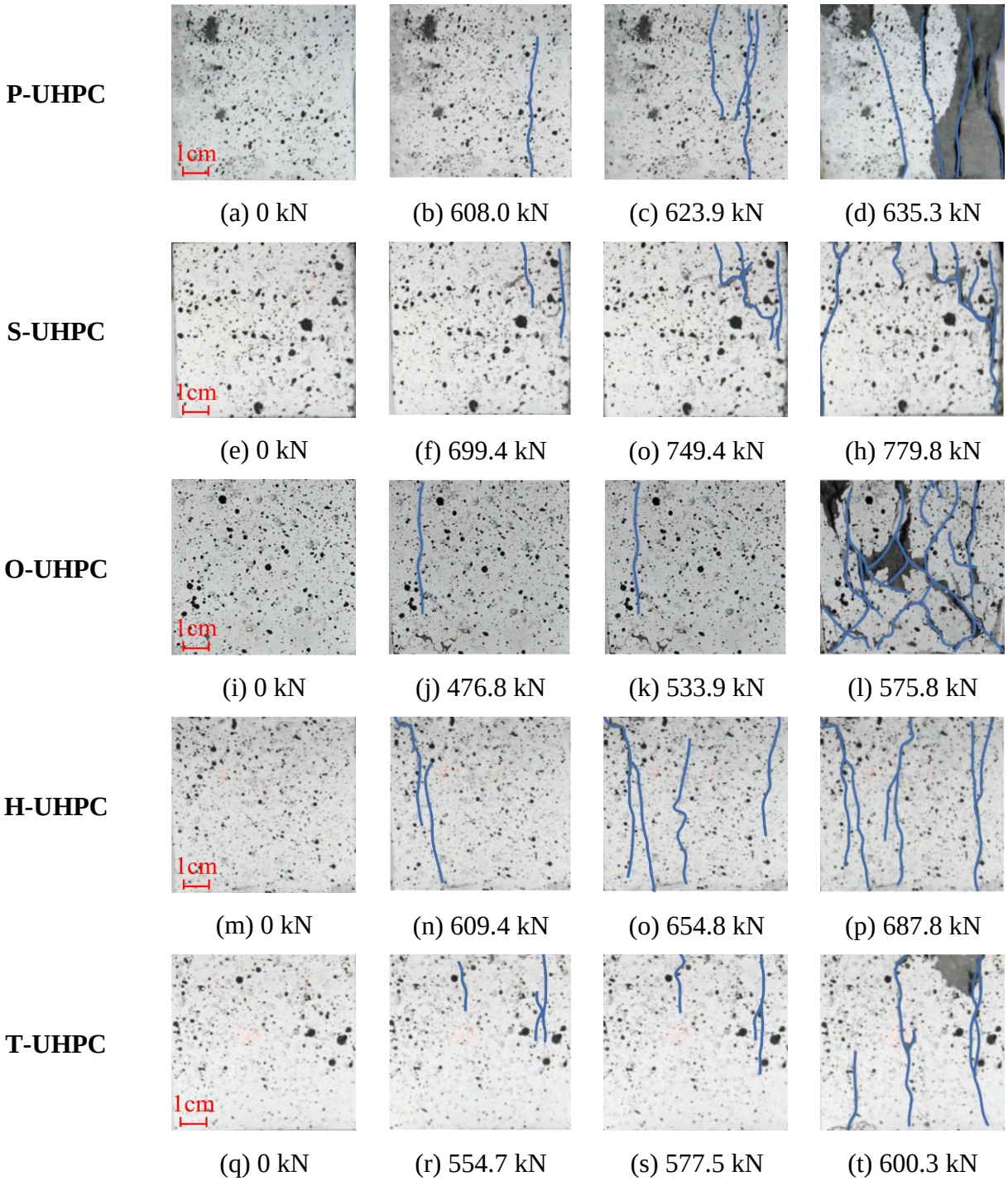

Fig. 6. Cracking process of specimens under uniaxial compression.

Similar as P-UHPC, the long longitudinal crack of O-UHPC initiated at 476.8 kN (82.8% P_u), as shown in Fig. 6j. After that, more cracks can be observed and bifurcate along the diagonal struts of octet structures as the PLA lattice first deformed due to low elastic modulus, followed by debonding

concrete from lattice structure along the bi-diagonal direction. In addition, plain concrete was prone to developing diagonal cracks as bearing compression because the end face of the concrete was subjected to friction under compression [79]. For H-UHPC (Fig. 6m-p), the crack initiation took place near the border of the specimen as the load reached 609.4 kN (88.6% P_u), followed by the appearance of multiple longitudinal cracks and crack propagation. The specimen failure happened at the loading of 687.8 kN. Compared to H-UHPC, less cracks can be observed on T-UHPC with relatively smaller crack width. The cracks were mainly concentrated on the connection location of triangular unit cells, implying the weakest reinforcement in T-UHPC. In comparison with O-UHPC, H-UHPC and T-UHPC had higher crack resistance. This is because the NPR effect of the re-entrant lattice reinforcement led to a biaxial compression of concrete filler during the compressive process, hindering the development of micro-cracks [52]. As observed, the cracks of all specimens first initiated longitudinally at the border of the specimens, regardless of reinforcement type.

3.1.2 Stress-strain curves

Fig. 7 shows the static compressive stress-strain curves of all specimens. Apart from P-UHPC specimens that exhibited brittle failure as the strain reached about 0.3%, the stress-strain curves of all other reinforced UHPC specimens followed a similar trend with a rapid rise to the peak stress, followed by a gentle downward until the final failure. S-UHPC had an obviously prolonged strain-softening stage because of the steel fibre bridging effect that delayed the crack development [64]. Similarly, for lattice reinforced UHPC, the uniform tessellated lattice possessed superior ability on controlling the crack initiation and propagation. The strain at the peak stress of S-UHPC was smallest (i.e., 0.45%), followed by that of T-UHPC, H-UHPC and O-UHPC which were 0.72%, 0.81% and 0.92%, respectively. Compared with S-UHPC, lattice reinforced UHPC showed larger strain at peak stress and relatively more smooth curves, suggesting that PLA lattice reinforcement can delay the coalition of microcracks to generate and enlarger zone damage [80]. H-UHPC presented better stress-strain behaviour compared to T-UHPC, consistent with previous studies [16, 53] that re-entrant honeycomb reinforced composites usually have better compressive performance than other lattice reinforced composites.

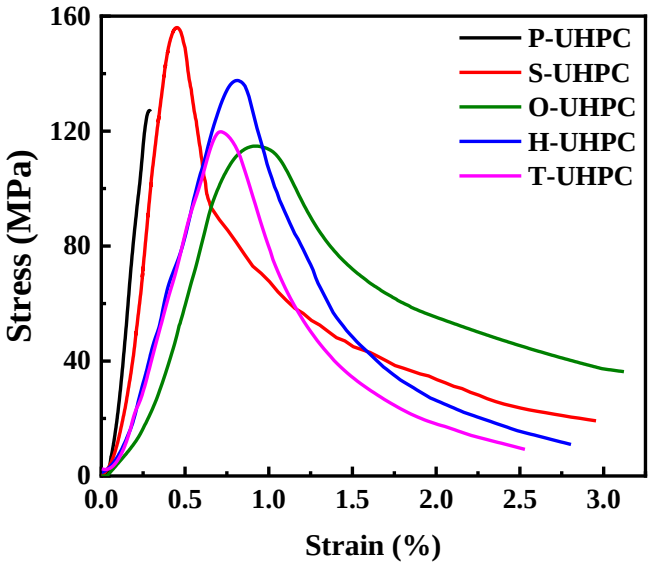

Fig. 7. Static compressive stress-strain curves of all specimens.

3.1.3 Compressive strength

Fig. 8 illustrates the static compressive strength of all specimens. S-UHPC had the highest compressive strength of 156.0 MPa, which was 13.4%, 22.7%, 29.9% and 35.4%, respectively higher than that of H-UHPC, P-UHPC, T-UHPC and O-UHPC, implying the obvious steel fibre bridging action for S-UHPC. The incorporation of PLA octet lattice and re-entrant triangular lattice led to a 9.4% and 5.5% respectively reduction in compressive strength of P-UHPC. However, the compressive strength of H-UHPC was enhanced by 8.3%, which can be ascribed to the excellent auxetic properties of re-entrant honeycomb lattice that laterally constrained the concrete deformation in compression and formed a biaxial compression state of the composite [5]. Thus, the load-bearing capacity of the composite can be improved. The re-entrant triangular structure had relatively short but thick struts due to the same volume fraction, leading to insignificant auxetic behaviour [44]. Hence, the compressive strength of T-UHPC was dominated by material properties of PLA lattice.

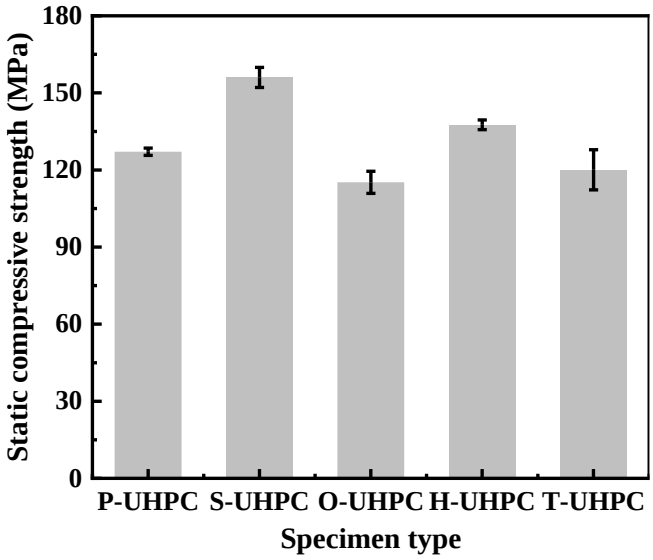

Fig. 8. Static compressive strength of all specimens.

3.1.4 Static compressive deformation

As seen in Fig. 7, O-UHPC exhibited the highest ultimate strain of 3.12%, followed by S-UHPC, H-UHPC, T-UHPC and P-UHPC at 2.96%, 2.81%, 2.53% and 0.29%. It was indicated that octet lattice had an obvious improvement in the ductility of concrete, which was more superior than that of auxetic lattice. In addition, the high ductility of steel fibre reinforced UHPC was derived from the bridging effect of the fibres across cracks, which restricted the crack development through a large amount of energy dissipation [81]. The strains at peak stress of S-UHPC, O-UHPC, H-UHPC and T-UHPC were 0.45%, 0.92%, 0.81% and 0.72%, respectively, which were higher than that of P-UHPC (i.e., 0.29%). The reinforcement improved the strain at peak stress of concrete and broadened the range of engineering application and the slender struts in lattice greatly increased the concrete ductility.

3.1.5 Dissipated energy

The energy dissipation of reinforced concrete was defined by the sum of the energy dissipated by concrete matrix and reinforcing phase [82]. The compressive dissipated energy of concrete specimens can be calculated by the area within the compressive stress-strain curves. The dissipated energy of P-UHPC was 74.1 J because P-UHPC without reinforcement lost its loading capacity quickly after reaching the peak stress. In comparison, the dissipated energy of S-UHPC, O-UHPC, H-UHPC and T-UHPC was higher by 597%-1035.8%, amounting to 699.3 J, 841.2 J, 660.3 J and 517.4 J, respectively, due to the reinforcement including steel fibres and PLA struts in concrete specimens absorbed a large amount of energy by tensile elongation during the crack development and provided reliable bonding and residual stresses even after the cracking surface penetrated the specimens. S-UHPC and H-UHPC dissipated the similar amount of energy, while O-UHPC and T-UHPC respectively showed the highest and T-UHPC the lowest energy dissipation. This indicated that the lattice reinforcement greatly enhanced the energy absorption of the specimen. O-UHPC had higher energy dissipation compared with H-UHPC and T-UHPC, which can be attributed to that the uniform slender struts presented higher energy absorption capacity than the concentrated structural form of auxetic lattice with the same volume fraction of the lattice in UHPC under static compressive loading.

3.2 Dynamic compressive behaviour

3.2.1 Failure patterns

Fig. 9 displays the dynamic compressive failure patterns of all specimens. Apart from S-UHPC, the failure patterns of P-UHPC and other lattice reinforced UHPC specimens exhibited similar features in terms of damage level with the increase of strain rate: increasing from almost complete specimen at the strain rate of 34.8 s^{-1} (Fig. 9a, f, k, p and u) to fragmentary failure as the strain rate reached 134.7 s^{-1} (Fig. 9e, j, o, t and y). This is because the short impact time at high strain rate cannot guarantee the internal micro-crack development of concrete specimens in spite of the generation of a large number of cracks [83]. S-UHPC retained the core integrity under different strain rates, which

can be ascribed to the lower elastic modulus of UHPC, resulting in the first large deformation of concrete under dynamic compression. The rapidly developed cracks in concrete were bridged by steel fibres, leading to the core integrity of the specimens. In comparison, PLA had low elastic modulus and was prone to deformation, resulting in concrete debonding from lattice.

At 34.8 s^{-1}, nearly all specimens kept complete, while the edges of T-UHPC appeared slight detachment. As the strain rate went up to about 59.7 s^{-1}, cracks occurred on the surface of all specimens but the core area kept relatively complete. T-UHPC and H-UHPC had similar but slighter fragment spalling (Fig. 9q and v) at the edges as P-UHPC (Fig. 9b), which can be ascribed to the weak joints of re-entrant triangular unit cells, leading to the weak reinforcement effects at the edges of whole lattice structure. When the strain rate reached around 86.7 s^{-1}, more fragmental split can be observed in P-UHPC, O-UHPC, T-UHPC and H-UHPC (Fig. 9c, r and w), while S-UHPC showed slight detachment at the edges (Fig. 9h and m). More cracks formed and developed in all concrete specimens. With the further rise of strain rate to around 108.5 s^{-1}, the outer area of all concrete specimens was destroyed of different levels, while the cracks developed towards the middle area. Obvious cracking penetration happened through the edges of P-UHPC, O-UHPC and T-UHPC (Fig. 9d, n and x). H-UPHC and S-UHPC kept a relatively complete state (Fig. 9i and s). It is noteworthy that when PLA lattice reinforced UHPC was destroyed the fracture surface shape was highly coincident with the strut path (Fig. 9n, s and x), indicating that the cracks were caused by concrete debonding from the lattice [65]. P-UHPC and O-UHPC were broken into multiple fragments at the strain rate of strain rate to around 134.7 s^{-1} (Fig. 9e). T-UHPC remained relatively complete lattice along with a few matrices, while most of the longitudinal joints of unit cells were broken (Fig. 9y). The PLA lattice exhibited weak restrictions on crack development of UHPC under high strain rates. In comparison, re-entrant triangular lattice played an essential role in reinforcing the adjacent internal concrete, and meanwhile, the internal concrete could be constrained by the external concrete under dynamic compression. Besides, the external concrete could be broken due to lack of restraints caused by both geometrical limitation and weak link failure. The NPR effect of auxetic lattice resulted in a biaxial compression status, delaying the formation and propagation of cracks in UHPC.

The worst dynamic compressive failure patterns took place in P-UHPC compared to other reinforced UHPC at various strain rates, indicating that the crack development and the transverse deformation of concrete can be effectively restrained by the addition of steel fibres [64]. Besides, S-UHPC presented superior dynamic compressive failure patterns at all strain rates because of the better reinforcement effects of steel fibres against PLA lattice. The steel fibres were uniformly distributed in concrete, whilst the auxetic and non-auxetic lattice structures usually had weak cross-sections, leading to about the through cracks and overall damage of the structure at high strain rates.

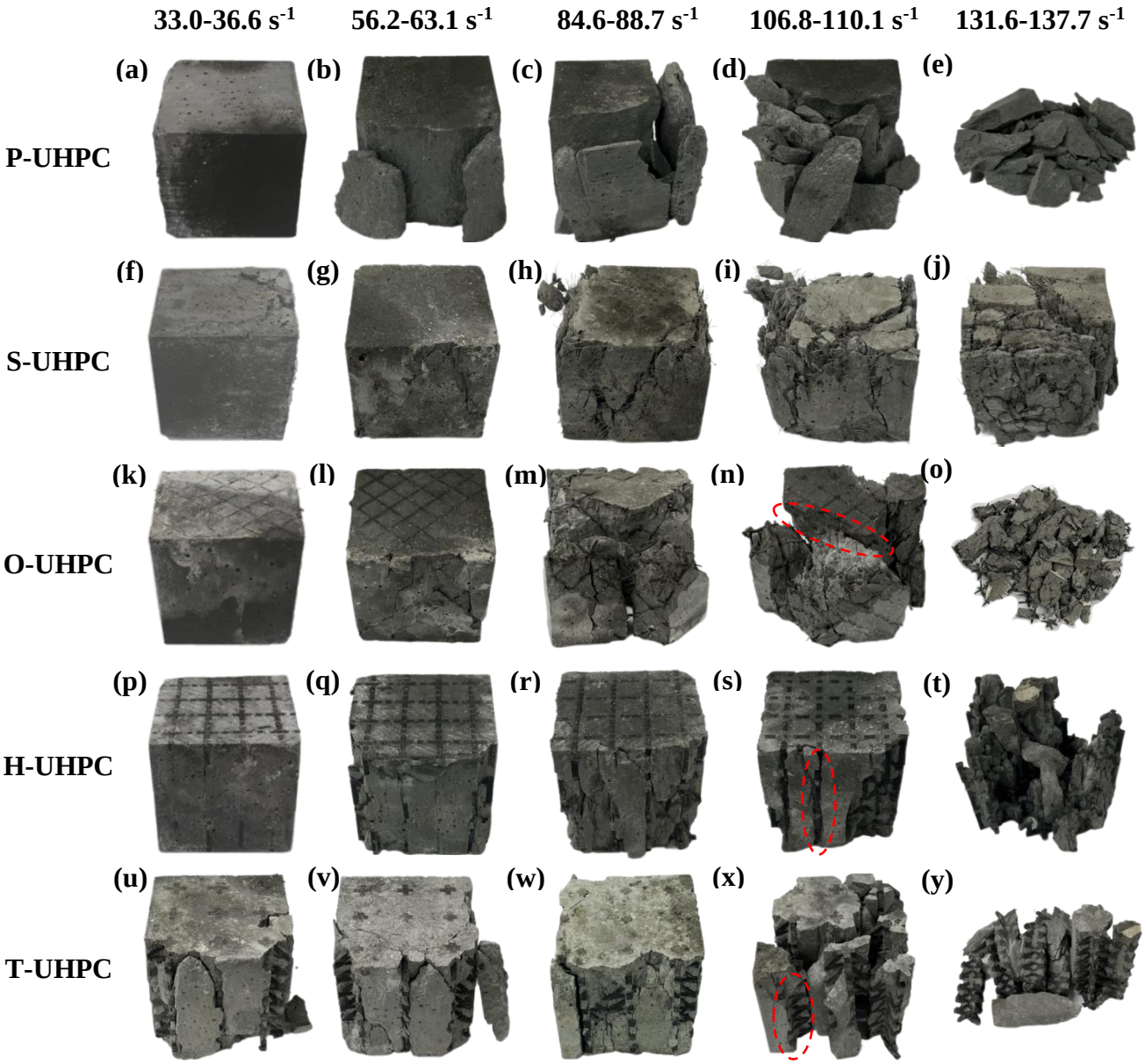

Fig. 9. Failure patterns of different specimens at various strain rates (Note: the red circles refer to the cracks caused by lattice debonding).

3.2.2 Stress-strain curves

Fig. 10 presents the stress-strain curves for all specimens at various strain rates (about 34.8-134.7 s^{-1}), indicating the same trend for them (except P-UHPC), mainly consisting of three stages: a linear elastic rise region, a plastic region due to the initiation and development of micro-cracks in concrete, and a softening region after reaching the peak stress. During the softening stage, a short stress plateau was interspersed in the rapid descent stage, where the cracks in concrete further developed and eventually concrete was destroyed. The stress plateau can be ascribed to the steel fibre bridging effect and PLA lattice reinforcement effect. P-UHPC showed the pure rapid descent curve in the strain-softening stage due to lack of reinforcement in P-UHPC to resist the crack development.

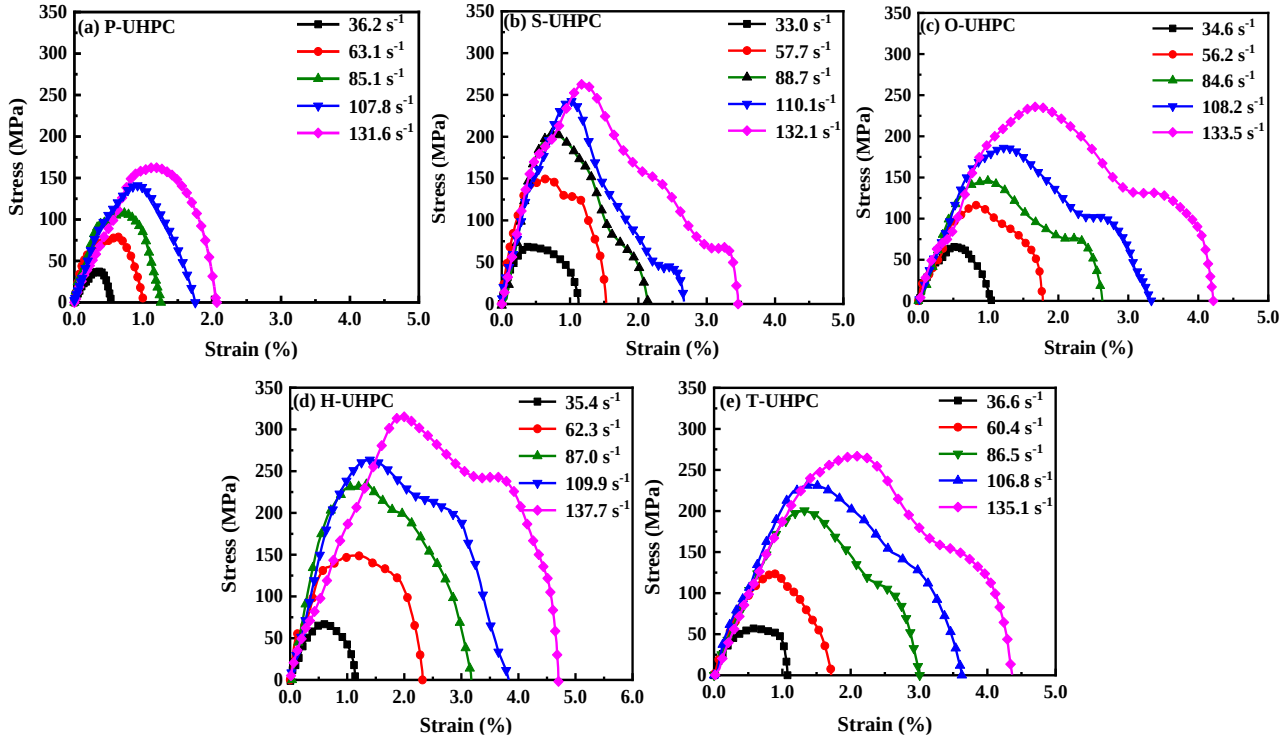

Fig. 10. Effect of strain rate on dynamic compressive stress-strain curves of (a) P-UHPC, (b) S-UHPC, (c) O-UHPC, (d) H-UHPC, and (e) T-UHPC.

Table 6 summarises the measured dynamic properties of all specimens, which indicates a significant enhancement of dynamic compressive strength with the increasing strain rate. As the strain rate went up, the dynamic compressive strength of P-UHPC, S-UHPC, O-UHPC, H-UHPC and T-UHPC was increased by 11.2-28.2%, 9.2-40.5%, 5.6-70.7%, 41.9-91.8% and 39.1-85.0%, respectively compared to their static compressive strengths, which can be attributed to the strain rate effect under dynamic compression. The strain rate effect stems from the theory of energy balance under dynamic impact at high strain rates or the lateral inertia effect on the specimen surface [84-87]. When a high strain rate was applied, the striker bar showed a high impact velocity with a short impact time, generating a huge kinetic energy to impact the specimen. Thus, to balance and absorb this energy, the strain energy inside the specimen increased dramatically, resulting in the micro-crack development. As the energy required for microcrack propagation was lower than that needed for crack initiation, the micro-cracks of concrete cannot be sufficiently propagated within a very short impact time before final failure, while more new micro-cracks were generated to absorb more energy [60]. Therefore, the dynamic compressive strength went up with the increasing impact velocity and strain rate, which verified the failure patterns of the specimens (Fig. 9). The dynamic compressive stress enhanced significantly, thereby providing energy for crack formation under high strain rates.

Table 6 Summary of dynamic properties of all specimens obtained from SHPB test.

Symbol	Average strain rate (s^{-1})	Dynamic compressive	DIF	Strain at peak stress ($\times10^{-3}$)	Ultimate strain ($\times10^{-3}$)	Fracture energy (J)	Total energy (J)

		strength (MPa)					
P-UHPC	36.2	37.2±3.7	0.29±0.029	3.52±0.89	5.29±1.92	24.0±2.9	37.3±3.2
	63.1	78.8±7.2	0.62±0.057	6.38±1.02	10.06±2.03	95.1±4.3	157.1±7.2
	85.1	107.7±5.9	0.85±0.047	7.05±1.11	12.55±2.29	138.9±12.2	260.9±29.1
	107.8	140.9±8.9	1.11±0.070	9.17±1.12	17.55±3.17	208.9±20.1	429.9±34.3
	131.6	162.4±6.1	1.28±0.048	11.92±1.57	20.68±3.45	314.1±28.9	612.0±40.9
S-UHPC	33.0	57.0±0.9	0.37±0.005	4.01±0.61	11.36±1.22	43.1±3.9	132.9±5.1
	57.7	124.9±4.8	0.80±0.031	6.86±0.69	15.29±1.49	143.5±9.2	356.1±17.0
	88.7	170.3±4.1	1.09±0.026	7.71±0.85	21.50±1.80	227.2±12.5	576.3±21.4
	110.1	193.2±7.6	1.24±0.049	10.20±1.11	26.68±2.14	357.0±28.9	775.7±47.2
	132.1	219.2±6.5	1.41±0.042	12.23±1.26	34.60±2.56	502.1±33.4	1412.5±52.3
O-UHPC	34.6	54.9±4.9	0.48±0.036	4.96±0.51	10.54±1.59	47.1±3.0	104.7±9.1
	56.2	97.0±8.0	0.84±0.059	8.26±0.81	17.79±1.90	140.6±7.3	323.1±19.2
	84.6	121.7±12.2	1.06±0.091	9.93±1.21	26.31±3.11	215.3±16.9	564.8±31.2
	108.2	155.0±11.7	1.35±0.087	12.63±1.33	33.30±3.27	329.6±21.5	878.7±49.4
	133.5	196.6±14.1	1.71±0.104	16.69±1.31	42.16±3.52	470.0±33.8	1564.8±64.5
H-UHPC	35.4	55.9±4.6	0.41±0.033	6.01±0.55	11.47±1.14	49.5±6.3	123.4±14.9
	62.3	124.1±2.6	0.90±0.019	11.70±0.62	23.20±1.32	281.7±9.0	660.7±27.1
	87.0	195.2±8.9	1.42±0.064	12.90±0.89	31.75±1.82	485.8±23.3	1153.0±41.9
	109.9	219.6±11.0	1.60±0.080	13.97±1.11	38.32±2.30	540.3±26.9	1550.3±48.1
	137.7	262.7±6.4	1.91±0.047	19.98±1.25	47.02±2.57	775.3±38.1	2254.3±75.2
T-UHPC	36.6	47.5±4.4	0.40±0.037	6.15±0.63	10.76±1.23	58.0±6.7	109.1±13.3
	60.4	102.7±5.7	0.86±0.047	8.93±0.73	17.15±1.41	162.8±14.6	315.3±30.2
	86.5	167.1±9.7	1.39±0.081	13.23±0.85	30.10±1.98	368.0±28.9	867.1±45.0
	106.8	193.4±12.4	1.61±0.103	14.14±1.22	36.27±2.41	422.0±30.4	1138.4±51.2
	135.1	222.2±14.0	1.85±0.117	20.94±1.35	43.63±2.88	690.0±41.9	1688.9±77.3

Fig. 11 shows the effects of specimen type and strain rate on the dynamic compressive strength. At the strain rate of around 34.8 s^{-1}, S-UHPC had the highest dynamic compressive strength of 57.0 MPa, followed by H-UHPC and O-UHPC of 55.9 and 54.9 MPa, respectively. Different from the static compressive findings, the presence of re-entrant triangular lattice led to a rise in dynamic compressive strength of concrete compared to P-UHPC. Multiple cracks were developed in lattice reinforced UHPC under dynamic compression, where the PLA struts played the same role as fibres in concrete specimens, and the stepped cracks were caused by concrete debonding. They both absorbed more energy for microcrack propagation and thus improved the dynamic compressive strength of the specimen.

The dynamic compressive strength of H-UHPC was significantly higher than that of other specimens at high strain rates (i.e., around 86.7 s^{-1}, 108.5 s^{-1} and 134.7 s^{-1}), where H-UHPC exhibited the greatest strength at each strain rate (i.e., 195.2 MPa, 219.6 MPa and 262.7 MPa, respectively). T-UHPC with low static compressive strength due to the weak joints of lattice structure also had a

similarly high dynamic compressive strength to S-UHPC at high strain rates. However, the strength of O-UHPC was about 20.8-29.5% lower than that of S-UHPC. In addition to the bridging effect of PLA struts in 3D lattices, the enhanced dynamic strength at high strain rates can be mainly ascribed to the NPR effect, allowing the specimens to enter into a bi-directional compressive state upon impact. Meanwhile, the specimens became denser, which was also beneficial to the compressive strength. Furthermore, as the crack width increased, the geometry of 3D lattices prevented the struts from being pulled out owing to the roughness of the interface, resulting in more reliable reinforcement and fuller utilisation of PLA tensile properties compared to fibres that were prone to be pulled out [88].

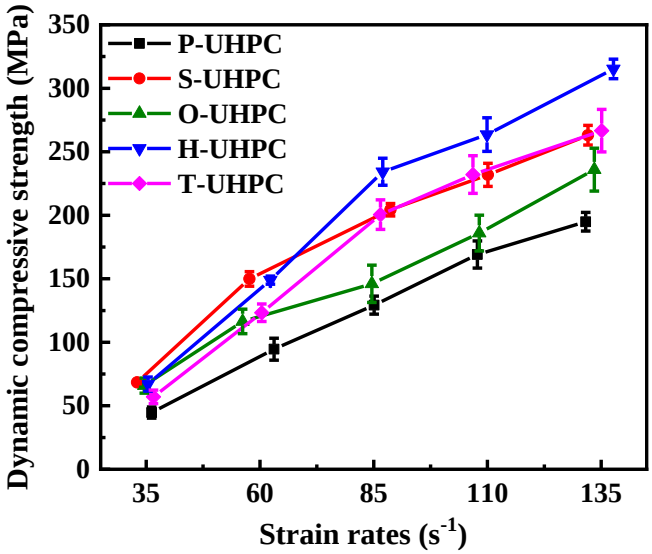

Fig. 11. Effect of specimen type on dynamic compressive strength under different strain rates.

3.2.3 Dynamic increase factor

The dynamic increase factor (DIF), which is defined as the ratio of dynamic and static compressive strengths, is commonly used to evaluate the strain rate dependence of materials. As summarised in Table 6, when the strain rate was above 106.8 s^{-1}, DIFs were higher than 1 for all specimens, indicating that after exceeding a certain impact velocity, the dynamic compressive strength was higher than the static compressive strength. In addition, DIFs gradually went up with the increase of strain rate. It was reported that the logarithm of DIF and strain rate are linearly and positively correlated, with the ratio being a necessary parameter to ensure correct structural design [89]. DIFs of reinforced UHPC were much higher than that of P-UHPC at the similar strain rate, which can be attributed to that the fibre or lattice reinforcement improved the dynamic compressive strength enhancement. As displayed in Fig. 12, the auxetic lattice reinforced UHPC exhibited higher DIFs under high strain rate impact in comparison with S-UHPC and O-UHPC. This is because compared to the steel fibre bridging effect after the generation of cracks, the PLA lattice confined the matrix during the whole impact process. Moreover, the auxetic PLA lattice with low elastic modulus presented higher bi-axial deformation under same compression, which confined the deformation of matrix and delayed the crack development of UHPC. The confinement effect of lattice was

accordingly enhanced with the rising strain rate.

Fig. 13 shows the fitted linear curves of DIF against strain rate logarithm for all specimens. All curves indicated a similar upward trend. The accuracy of the fitted curves can be assessed using the correlation coefficients (R^2) given in Table 7, which were all above 0.9, indicating the good reliability of all fitted curves. It can be observed that the fitted straight lines of the two specimens with auxetic lattices possessed a higher slope, implying that the addition of auxetic lattice held a more positive effect on dynamic compressive strength of concrete compared to steel fibres.

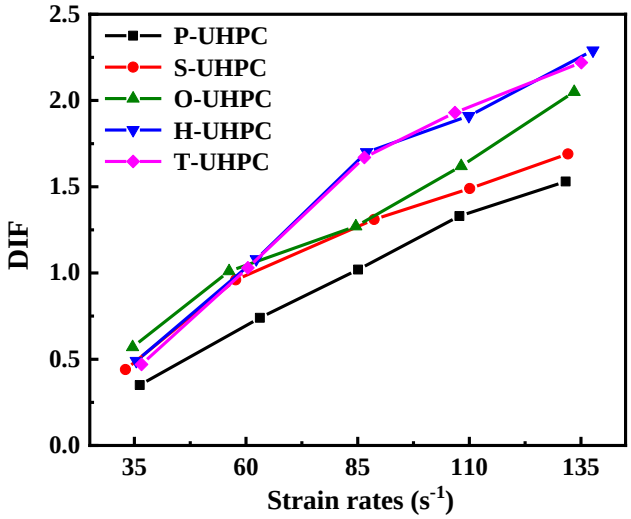

Fig. 12. Relationship between DIF and strain rate for all specimens.

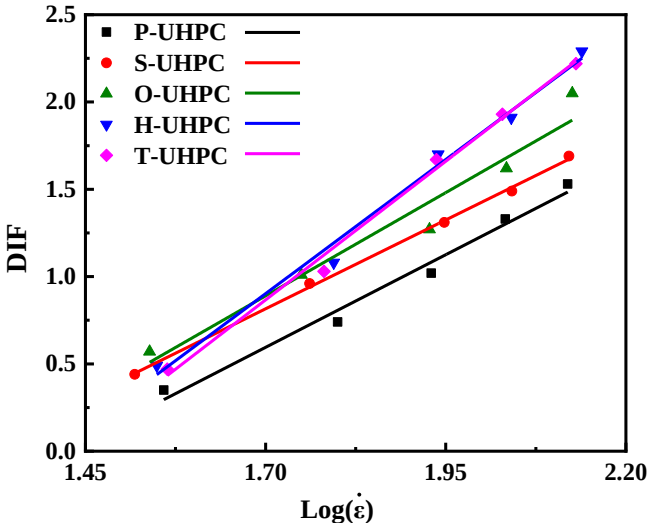

Fig. 13. Fitted linear curves of DIF against logarithm of strain rate.

Table 7 Summary of the fitted DIF equations for different specimens.

Symbol	Fitted equation of DIF	Correlation coefficient (R^2)
P-UHPC	DIF=2.122log$\dot{\varepsilon}$-3.012	0.978
S-UHPC	DIF=2.035log$\dot{\varepsilon}$-2.645	0.998
O-UHPC	DIF=2.365log$\dot{\varepsilon}$-3.131	0.942
H-UHPC	DIF=3.072log$\dot{\varepsilon}$-4.320	0.985
T-UHPC	DIF=3.095log$\dot{\varepsilon}$-4.531	0.991

3.2.4 Dynamic compressive strain

The strain at peak load and ultimate strain presented in Fig. 14 reflected the deformability of the specimen at the time of full crack development and final failure, respectively [89], which both raised with the increasing strain rate. A comparison of the strain variables between the two figures indicated that the ultimate strain of reinforced UHPC was 112-183% higher than that at the peak stress under all strain rates. The bridging effect of fibres or PLA struts at the cracks prolonged the strain-softening region, which improved the toughness and energy absorption of UHPC [88].

Although the stress of S-UHPC was much higher than that of P-UHPC at the same strain rate, the strain under peak load and ultimate strain were only 2.5-11.2% and 52.0-116.7% higher, respectively. On the contrary, both strains for three types of specimens with 3D lattices were higher than that of S-UHPC, especially for the two types of UHPC reinforced with auxetic lattices. This is consistent with the findings by Brian Salazar et al. [65]. It was observed that PLA struts resisted cracking after the incorporation of 3D lattices, while the lattice paths lengthened as cracks were mainly caused by lattice debonding, which facilitated the improvement of ductility of concrete. The dynamic strain of auxetic lattice reinforced UHPC was higher than that of O-UHPC, which can be attributed to the restriction effects of NPR lattices on the crack development. The resulting biaxial compression of UHPC also prevented the local failure.

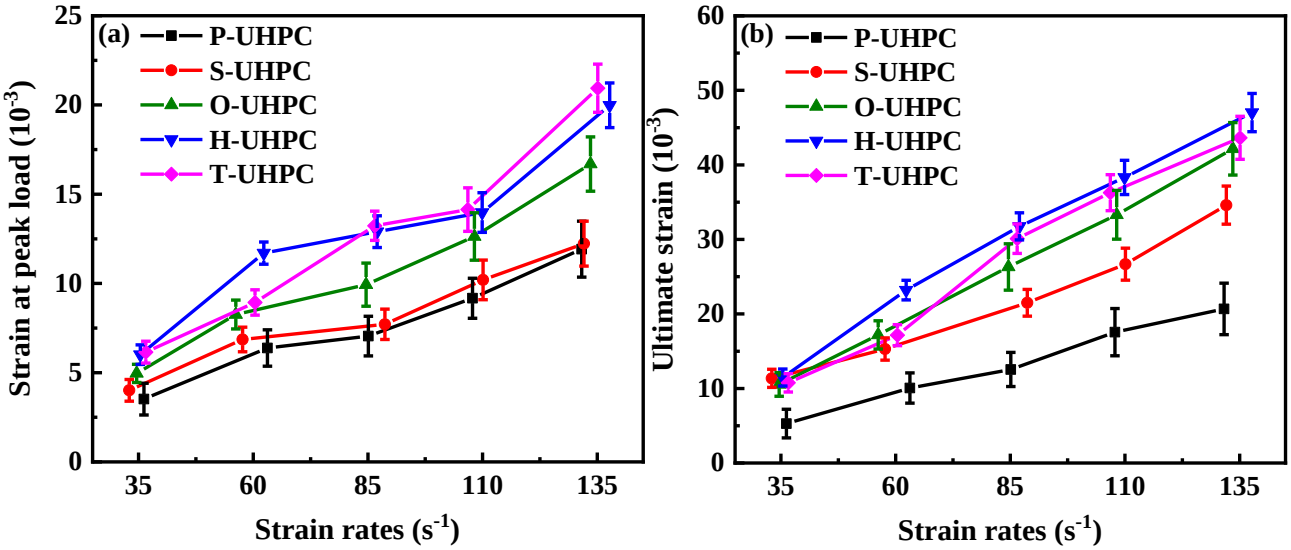

Fig. 14. Effect of specimen type on (a) strain at peak load, and (b) ultimate strain under different strain rates.

3.2.5 Dissipated energy

In SHPB test, the energy dissipation of specimens was closely related to dynamic compressive stress and failure patterns. Both dynamic compressive strength and the energy absorption capacity increased accordingly with the growth of strain rates, while the microcracks and large cracks in the failed specimens multiplied. It can be clearly seen from Fig. 15 that both fracture energy and total energy were enhanced with increasing strain rate. The increase in energy absorption capacity was attributed to that

more cracks were generated in the specimens within a very limited loading time at higher strain rates, which was well consistent with the failure pattern in Fig. 9.

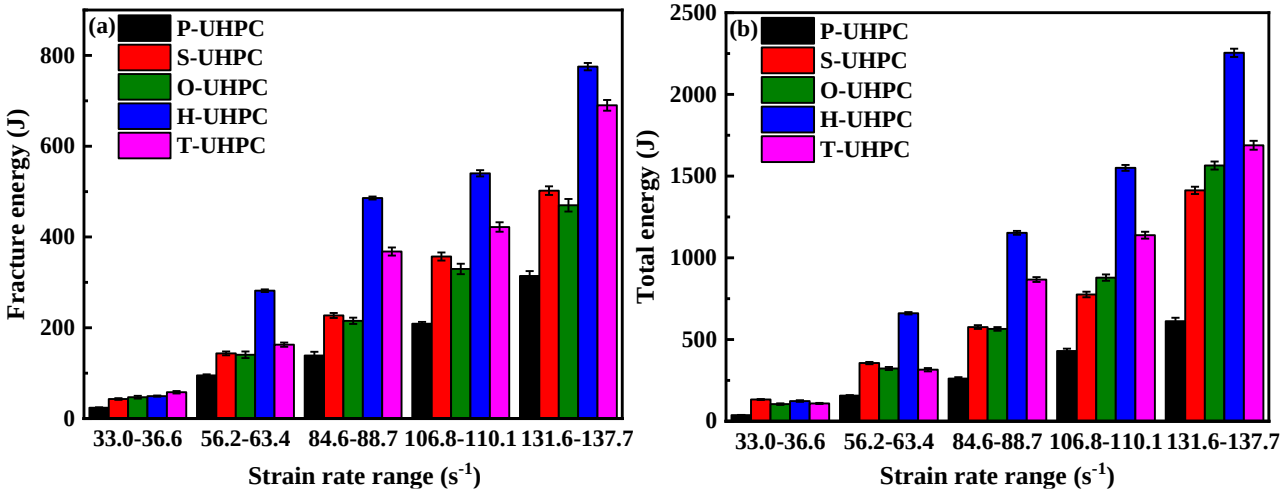

Fig. 15. Dynamic energy absorption capacity of UHPC in terms of (a) fracture energy, and (b) total energy under different strain rates.

Fracture energy represents all the energy absorbed by the specimen before the peak stress in dynamic compressive test, which can be calculated by multiplying the area under the stress-strain curve at the peak stress by the volume of the specimen [64]. T-UHPC and H-UHPC exhibited the highest fracture energy under high strain rate impact, reaching 775.3 J and 695.0 J, respectively. It can be explained by the fact that the failure patterns of UHPC specimens at high strain rates changed from local damage to global fragmentation, and thus more NPR units were utilised. The additional NPR effects resulted in bi-directional compression and denser structure, thus increasing the peak stress and fracture energy required for crack initiation. The fracture energy of S-UHPC and O-UHPC was basically the same, fluctuating in the range of 6.8%, much lower than that of H-UHPC and T-UHPC. It was found that the NPR of auxetic lattice showed a good enhancement on the resistance of UHPC to cracking, thereby increasing the fracture energy.

The total energy absorption of UHPC specimens tested by SHPB, i.e., $W_{total}(t)$, was calculated by the difference in energy of incident, reflected and transmitted waves, as expressed below [90, 91]:

$$W_{total}(t) = W_1(t) - W_2(t) - W_3(t) \tag{2}$$

$$W_i(t) = EC_0A_0\int_0^t \varepsilon^2(t)dt \tag{3}$$

where $W_1(t)$, $W_2(t)$ and $W_3(t)$ denote the energy of incident wave, reflected wave and transmitted waves, respectively, and the subscript *i* (= 1, 2, 3) stands for different types of wave.

The total energy consists of fracture energy and post-crack energy. The post-crack energy denotes the energy absorbed by the deformation of fibres or lattice through cracking after the initiation of crack, which is the main part of the energy absorbed by reinforced concrete [83, 91]. For concrete reinforced with 3D PLA lattice, the energy was dissipated by crack generation, along with lattice

deformation and pulling out in the fracture zone. As seen in Fig. 15b, the lattice reinforced UHPC presented similar total energy as steel fibre reinforced UHPC at around 34.8 s^{-1}, indicating that the lattice provided the similar confinement effects on crack development as fibres under low strain rate, where few NPR effects can be observed. As the strain rate raised to higher than 59.7 s^{-1}, the auxetic lattice reinforced UHPC showed higher energy dissipation compared to O-UHPC and S-UHPC. H-UHPC had the highest total energy and post-crack energy at high strain rates, which were 2254.3 J and 1479.0 J. Large deformation, sliding and friction took place in PLA lattice, achieving a high energy absorption compared to fibre reinforced UHPC. Additionally, UHPC matrix turned into a bi-axial compressive status under high velocity impact, limiting the crack initiation and propagation. Matrix was deboned from the struts, while the cracking paths overlapped the struts and performed stepped oblique along with the longest struts compared with the straight oblique cracks in S-UHPC [60, 65]. H-UHPC presented much higher energy dissipation in comparison with T-UHPC, indicating the high tensile deformation of lattice structure and friction between the lattice and matrix. Cracking in T-UHPC mostly happened at weak joints, resulting in mostly vertical cracks, which limited the number of tensioned struts and thus reduced the energy absorption capacity. Moreover, the total energy of O-UHPC exceeded that of S-UHPC at high strain rates, under the premise that its fracture energy was less than that of S-UHPC. The enhancement in post-crack energy of concrete by 3D lattice was more significant than fibres, as the uniformed geometry of 3D lattice can compensate for the defect of fibre, fully exploiting the energy absorption ability of struts.

4. Conclusions

In this study, the static and dynamic compressive behaviour of 3D octet, re-entrant honeycomb and triangular lattice reinforced ultra-high performance concrete (UHPC) in comparison with the reference plain UHPC and steel fibre reinforced UHPC were experimentally investigated. Based on the obtained experimental results, the following main conclusions can be drawn:

- H-UHPC had a 14.6-19.4% higher static compressive strength than O-UHPC and T-UHPC. Although the incorporation of PLA material had a negative impact on compressive strength, the bi-directional compression status of the composites due to auxetic lattices provided additional support to UHPC matrix, which compensated for the strength loss caused by the weak material. O-UHPC exhibited the highest static ultimate strain of 3.12% and dissipated energy of 841.2 J, which were 5.4-23.3% and 20.3-62.6% respectively higher than that of H-UHPC, S-UHPC and T-UHPC. The uniform slender struts of O-UHPC had higher ductility and energy absorption capacity compared to auxetic lattice with weak cross-section in P-UHPC.
- With the increase of strain rate, the failure patterns of P-UHPC and reinforced UHPC specimens looked similar. The damage of the specimens increasing from almost complete specimen at the strain rate of 34.8 s^{-1} to serious splitting and fractional failure as the strain rate reached 134.7 s^{-1}.

The short impact time at high strain rate cannot guarantee the internal micro-crack development of UHPC specimens in spite of the generation of a large number of cracks.

- S-UHPC presented the highest dynamic compressive strength at low strain rates, while auxetic lattice reinforced UHPC held the highest dynamic strength at high strain rates. The dynamic compressive strength of H-UHPC was much higher than that of other specimens at high strain rates. The NPR effect of lattice allowed the specimens to enter into a bi-directional compressive state and become denser upon impact, which was also beneficial to compressive strength. The dynamic compressive strength of all specimens went up with the increasing impact velocity and strain rate, which can be ascribed to the strain rate effect under dynamic compression.
- H-UHPC possessed the highest total energy and post-crack energy at high strain rates. The large deformation, sliding and friction of PLA lattice led to a high energy absorption and UHPC matrix turned into a bi-axial compressive status under high velocity impact, resisting the crack initiation and growth. Much higher energy dissipation occurred in H-UHPC compared to T-UHPC, indicating the high tensile deformation of lattice structure and friction between the lattice and matrix. The cracks in T-UHPC mostly appeared at weak joints, resulting in mostly vertical cracks, which limited the number of tensioned struts and thus reduced the energy absorption capacity.
- Among all lattice reinforced UHPCs, H-UHPC exhibited excellent static and dynamic compressive performance and was about 10% lighter than S-UHPC, suggesting its potential application in lightweight construction. The static elastic modulus and compressive strength of H-UHPC were lower than that of S-UHPC. In comparison with S-UHPC, H-UHPC had comparable compressive strength and energy dissipation at low strain rates (i.e., around 34.8^{-1}-59.7 s^{-1}), while the dynamic compressive behaviour was enhanced much more obviously at high strain rates (i.e., around 86.7 s^{-1}-134.7 s^{-1}). The confinement effect of auxetic lattice was accordingly improved with the rising strain rate. The difference in material properties of lattice reinforcement and typical steel fibre could affect the compressive behaviour of UHPC. The results obtained from this study indicated the significance and broad application of auxetic lattice reinforced concrete, while further development in incorporating different auxetic lattice into different concrete composites (e.g., metallic lattice reinforced concrete) is required.

Acknowledgements

The research was funded by the National Natural Science Foundation of China (No. 52178382), the Fundamental Research Funds for the Central Universities (No. N2201023), and Liaoning Provincial Natural Science Foundation (No. 2020-MS-089). M. Zhang gratefully acknowledges the financial support from the Engineering and Physical Sciences Research Council (EPSRC) under Grant No. EP/R041504/1 and the Royal Society under Award No. IEC\NSFC\191417.

References

[1] Chan N, Evans K. The mechanical properties of conventional and auxetic foams. Part I: compression and tension. J Cell Plast. 1999;35:130-65.
[2] Chan N, Evans K. The mechanical properties of conventional and auxetic foams. Part II: shear. J Cell Plast. 1999;35:166-83.
[3] Webber R, Alderson K, Evans K. A novel fabrication route for auxetic polyethylene, part 2: Mechanical properties. Polym Eng Sci. 2008;48:1351-8.
[4] Coenen V, Alderson K. Mechanisms of failure in the static indentation resistance of auxetic carbon fibre laminates. Phys Status Solidi B. 2011;248:66-72.
[5] Li T, Liu F, Wang L. Enhancing indentation and impact resistance in auxetic composite materials. Compos Part B. 2020;198:108229.
[6] Scarpa F, Giacomin J, Bezazi A, Bullough W. Dynamic behavior and damping capacity of auxetic foam pads. Smart Structures and Materials 2006: Damping and Isolation: SPIE; 2006. p. 215-21.
[7] Scarpa F, Ciffo L, Yates J. Dynamic properties of high structural integrity auxetic open cell foam. Smart Mater Struct. 2003;13:49.
[8] Scarpa F, Bullough W, Lumley P. Trends in acoustic properties of iron particle seeded auxetic polyurethane foam. Proc Inst Mech Eng, Part C: J Mech Eng Sci. 2004;218:241-4.
[9] Scarpa F, Smith F. Passive and MR fluid-coated auxetic PU foam–mechanical, acoustic, and electromagnetic properties. J Intell Mater Syst Struct. 2004;15:973-9.
[10] Choi J, Lakes R. Fracture toughness of re-entrant foam materials with a negative Poisson's ratio: experiment and analysis. Int J Fract. 1996;80:73-83.
[11] Yang W, Li Z-M, Shi W, Xie B-H, Yang M-B. Review on auxetic materials. J Mater Sci. 2004;39:3269-79.
[12] Evans KE, Alderson A. Auxetic materials: functional materials and structures from lateral thinking! Adv Mater. 2000;12:617-28.
[13] Prawoto Y. Seeing auxetic materials from the mechanics point of view: a structural review on the negative Poisson’s ratio. Comput Mater Sci. 2012;58:140-53.
[14] Kuribayashi K, Tsuchiya K, You Z, Tomus D, Umemoto M, Ito T et al. Self-deployable origami stent grafts as a biomedical application of Ni-rich TiNi shape memory alloy foil. Mater Sci Eng A. 2006;419:131-7.
[15] Luo C, Han CZ, Zhang XY, Zhang XG, Ren X, Xie YM. Design, manufacturing and applications of auxetic tubular structures: A review. Thin-Walled Struct. 2021;163:107682.
[16] Li T, Chen Y, Hu X, Li Y, Wang L. Exploiting negative Poisson's ratio to design 3D-printed composites with enhanced mechanical properties. Mater Des. 2018;142:247-58.
[17] Evans KE, Nkansah M, Hutchinson I. Auxetic foams: modelling negative Poisson's ratios. Acta Metall Mater. 1994;42:1289-94.

[18] Sanami M, Ravirala N, Alderson K, Alderson A. Auxetic materials for sports applications. Procedia Eng. 2014;72:453-8.
[19] Alderson K, Simkins V, Coenen V, Davies P, Alderson A, Evans K. How to make auxetic fibre reinforced composites. Phys Status Solidi B. 2005;242:509-18.
[20] Jiang L, Gu B, Hu H. Auxetic composite made with multilayer orthogonal structural reinforcement. Compos Struct. 2016;135:23-9.
[21] Choi J, Lakes R. Design of a fastener based on negative Poisson's ratio foam. Cell Polym. 1991;10:205-12.
[22] Jiang Y, Liu Z, Matsuhisa N, Qi D, Leow WR, Yang H et al. Auxetic mechanical metamaterials to enhance sensitivity of stretchable strain sensors. Adv Mater. 2018;30:1706589.
[23] Zhang SL, Lai YC, He X, Liu R, Zi Y, Wang ZL. Auxetic foam - based contact - mode triboelectric nanogenerator with highly sensitive self - powered strain sensing capabilities to monitor human body movement. Adv Funct Mater. 2017;27:1606695.
[24] Ugbolue SC, Kim YK, Warner SB, Fan Q, Yang C-L, Kyzymchuk O et al. The formation and performance of auxetic textiles. Part I: theoretical and technical considerations. J Text Inst. 2010;101:660-7.
[25] Wang Z, Hu H. Auxetic materials and their potential applications in textiles. Text Res J. 2014;84:1600-11.
[26] Ungureanu B, Achaoui Y, Enoch S, Brûlé S, Guenneau S. Auxetic-like metamaterials as novel earthquake protections. arXiv preprint arXiv:151008785. 2015.
[27] Brûlé S, Enoch S, Guenneau S. Emergence of seismic metamaterials: Current state and future perspectives. Phys Lett A. 2020;384:126034.
[28] Choi J, Lakes R. Analysis of elastic modulus of conventional foams and of re-entrant foam materials with a negative Poisson's ratio. Int J Mech Sci. 1995;37:51-9.
[29] Rad MS, Hatami H, Ahmad Z, Yasuri AK. Analytical solution and finite element approach to the dense re-entrant unit cells of auxetic structures. Acta Mech. 2019;230:2171-85.
[30] Gao Y, Wu Q, Wei X, Zhou Z, Xiong J. Composite tree-like re-entrant structure with high stiffness and controllable elastic anisotropy. Int J Solids Struct. 2020;206:170-82.
[31] Shen J, Liu K, Zeng Q, Ge J, Dong Z, Liang J. Design and mechanical property studies of 3D re-entrant lattice auxetic structure. Aerosp Sci Technol. 2021;118:106998.
[32] Grima JN, Evans KE. Auxetic behavior from rotating squares. 2000;19 (17):1563-5.
[33] Grima JN, Evans KE. Auxetic behavior from rotating triangles. J Mater Sci. 2006;41:3193-6.
[34] Grima JN, Alderson A, Evans K. Auxetic behaviour from rotating rigid units. Phys Status Solidi B. 2005;242:561-75.

[35] Gao Y, Wei X, Han X, Zhou Z, Xiong J. Novel 3D auxetic lattice structures developed based on the rotating rigid mechanism. Int J Solids Struct. 2021;233:111232.
[36] Ebrahimi H, Mousanezhad D, Nayeb-Hashemi H, Norato J, Vaziri A. 3D cellular metamaterials with planar anti-chiral topology. Mater Des. 2018;145:226-31.
[37] Ha CS, Plesha ME, Lakes RS. Chiral three-dimensional isotropic lattices with negative Poisson's ratio. Phys Status Solidi B. 2016;253:1243-51.
[38] Alderson A, Alderson KL, Attard D, Evans KE, Gatt R, Grima JN et al. Elastic constants of 3-, 4-and 6-connected chiral and anti-chiral honeycombs subject to uniaxial in-plane loading. Compos Sci Technol. 2010;70:1042-8.
[39] Grima JN, Gatt R. Perforated sheets exhibiting negative Poisson's ratios. Adv Eng Mater. 2010;12:460-4.
[40] Alderson A, Evans K. Microstructural modelling of auxetic microporous polymers. J Mater Sci. 1995;30:3319-32.
[41] Caddock B, Evans K. Microporous materials with negative Poisson's ratios. I. Microstructure and mechanical properties. J Phys D: Appl Phys. 1989;22:1877.
[42] Evans K, Caddock B. Microporous materials with negative Poisson's ratios. II. Mechanisms and interpretation. J Phys D: Appl Phys. 1989;22:1883.
[43] Shim J, Perdigou C, Chen ER, Bertoldi K, Reis PM. Buckling-induced encapsulation of structured elastic shells under pressure. Proc Natl Acad Sci USA. 2012;109:5978-83.
[44] Ren X, Shen J, Tran P, Ngo TD, Xie YM. Design and characterisation of a tuneable 3D buckling-induced auxetic metamaterial. Mater Des. 2018;139:336-42.
[45] Alderson A, Alderson K, Chirima G, Ravirala N, Zied K. The in-plane linear elastic constants and out-of-plane bending of 3-coordinated ligament and cylinder-ligament honeycombs. Compos Sci Technol. 2010;70:1034-41.
[46] Jiang Y, Li Y. 3D printed auxetic mechanical metamaterial with chiral cells and re-entrant cores. Sci Rep. 2018;8:1-11.
[47] Zahra T. Behaviour of 3D printed re-entrant chiral auxetic (RCA) geometries under in-plane and out-of-plane loadings. Smart Mater Struct. 2021;30:115011.
[48] Hsueh C-H, Schmauder S, Chen C-S, Chawla KK, Chawla N, Chen W et al. Handbook of mechanics of materials: Springer; 2019.
[49] Liu W, Wang N, Luo T, Lin Z. In-plane dynamic crushing of re-entrant auxetic cellular structure. Mater Des. 2016;100:84-91.
[50] Peng X-L, Soyarslan C, Bargmann S. Phase contrast mediated switch of auxetic mechanism in composites of infilled re-entrant honeycomb microstructures. Extreme Mech Lett. 2020;35:100641.

[51] Albertini F, Dirrenberger J, Sollogoub C, Maconachie T, Leary M, Molotnikov A. Experimental and computational analysis of the mechanical properties of composite auxetic lattice structures. Addit Manuf. 2021;47:102351.
[52] Zhang XG, Ren X, Jiang W, Zhang XY, Luo C, Zhang Y et al. A novel auxetic chiral lattice composite: Experimental and numerical study. Compos Struct. 2022;282:115043.
[53] Fíla T, Zlámal P, Jiroušek O, Falta J, Koudelka P, Kytýř D et al. Impact testing of polymer-filled auxetics using split Hopkinson pressure bar. Adv Eng Mater. 2017;19:1700076.
[54] Ngapeya GGC, Waldmann D. Overcome of bed-joint imperfections and improvement of actual contact in dry-stacked masonry. Constr Build Mater. 2020;233:117173.
[55] Zahra T, Dhanasekar M. Characterisation and strategies for mitigation of the contact surface unevenness in dry-stack masonry. Constr Build Mater. 2018;169:612-28.
[56] Xue Y, Wang W, Han F. Enhanced compressive mechanical properties of aluminum based auxetic lattice structures filled with polymers. Compos Part B. 2019;171:183-91.
[57] Novak N, Krstulović-Opara L, Ren Z, Vesenjak M. Mechanical properties of hybrid metamaterial with auxetic chiral cellular structure and silicon filler. Compos Struct. 2020;234:111718.
[58] Luo HC, Ren X, Zhang Y, Zhang XY, Zhang XG, Luo C et al. Mechanical properties of foam-filled hexagonal and re-entrant honeycombs under uniaxial compression. Compos Struct. 2022;280:114922.
[59] Zhong R, Ren X, Zhang XY, Luo C, Zhang Y, Xie YM. Mechanical properties of concrete composites with auxetic single and layered honeycomb structures. Constr Build Mater. 2022;322:126453.
[60] Zhou H, Jia K, Wang X, Xiong M-X, Wang Y. Experimental and numerical investigation of low velocity impact response of foam concrete filled auxetic honeycombs. Thin-Walled Struct. 2020;154:106898.
[61] Tzortzinis G, Gross A, Gerasimidis S. Auxetic boosting of confinement in mortar by 3D reentrant truss lattices for next generation steel reinforced concrete members. Extreme Mech Lett. 2022;52:101681.
[62] Scott BD, Park R, Priestley MJ. Stress-strain behavior of concrete confined by overlapping hoops at low and high strain rates. Journal Proceedings 1982. p. 13-27.
[63] Neville A, Aitcin P-C. High performance concrete—An overview. Mater Struct. 1998;31:111-7.
[64] Chen M, Si H, Fan X, Xuan Y, Zhang M. Dynamic compressive behaviour of recycled tyre steel fibre reinforced concrete. Constr Build Mater. 2022;316:125896.
[65] Salazar B, Aghdasi P, Williams ID, Ostertag CP, Taylor HK. Polymer lattice-reinforcement for enhancing ductility of concrete. Mater Des. 2020;196:109184.

[66] Aghdasi P, Williams ID, Salazar B, Panditi N, Taylor HK, Ostertag CP. An octet-truss engineered concrete (OTEC) for lightweight structures. Compos Struct. 2019;207:373-84.
[67] Common Portland Cement. Standard, Chinese National.
[68] Wu Z, Shi C, Khayat KH. Investigation of mechanical properties and shrinkage of ultra-high performance concrete: Influence of steel fiber content and shape. Compos Part B. 2019;174:107021.
[69] Wang X-T, Li X-W, Ma L. Interlocking assembled 3D auxetic cellular structures. Mater Des. 2016;99:467-76.
[70] Zhang H, Wang L, Zheng K, Bakura TJ, Totakhil PG. Research on compressive impact dynamic behavior and constitutive model of polypropylene fiber reinforced concrete. Constr Build Mater. 2018;187:584-95.
[71] Hao Y, Hao H. Dynamic compressive behaviour of spiral steel fibre reinforced concrete in split Hopkinson pressure bar tests. Constr Build Mater. 2013;48:521-32.
[72] Zhong H, Zhang M. Effect of recycled polymer fibre on dynamic compressive behaviour of engineered geopolymer composites. Ceram Int. 2022;48:23713-30.
[73] Naghdabadi R, Ashrafi MJ, Arghavani J. Experimental and numerical investigation of pulse-shaped split Hopkinson pressure bar test. Mater Sci Eng A. 2012;539:285-93.
[74] Chen WW, Song B. Split Hopkinson (Kolsky) bar: design, testing and applications: Springer Science & Business Media; 2010.
[75] Frew DJ, Forrestal MJ, Chen W. Pulse shaping techniques for testing brittle materials with a split Hopkinson pressure bar. Exp Mech. 2002;42:93-106.
[76] Vecchio KS, Jiang F. Improved pulse shaping to achieve constant strain rate and stress equilibrium in split-Hopkinson pressure bar testing. Metall Mater Trans A Phys Metall Mater Sci. 2007;38:2655-65.
[77] Ibrahim MA, Farhat M, Issa MA, Hasse JA. Effect of Material Constituents on Mechanical and Fracture Mechanics Properties of Ultra-High-Performance Concrete. ACI Mater J. 2017;114.
[78] Yang S, Tang Z, Zhong W, Wang S, Zhang R, Yao X. Effects of steel fibers on the dynamic properties and failure process of ultra-high performance concrete. J Build Eng. 2022;62:105415.
[79] Zhang T, Zhang M, Shen Y, Zhu H, Yan Z. Mitigating the damage of ultra-high performance concrete at elevated temperatures using synergistic flame-retardant polymer fibres. Cem Concr Res. 2022;158:106835.
[80] Choi S, Thienel K-C, Shah SP. Strain softening of concrete in compression under different end constraints. Mag Concr Res. 1996;48:103-15.
[81] Wu Z, Shi C, He W, Wang D. Static and dynamic compressive properties of ultra-high performance concrete (UHPC) with hybrid steel fiber reinforcements. Cem Concr Compos. 2017;79:148-57.

[82] Park H, Eom T. Energy dissipation capacity of reinforced concrete members. CTBUH 2004 Seoul Conference 2004. p. 378-84.
[83] Chen M, Chen W, Zhong H, Chi D, Wang Y, Zhang M. Experimental study on dynamic compressive behaviour of recycled tyre polymer fibre reinforced concrete. Cem Concr Compos. 2019;98:95-112.
[84] Xiao J, Li L, Shen L, Poon CS. Compressive behaviour of recycled aggregate concrete under impact loading. Cem Concr Res. 2015;71:46-55.
[85] Cotsovos D, Pavlović M. Numerical investigation of concrete subjected to compressive impact loading. Part 1: A fundamental explanation for the apparent strength gain at high loading rates. Comput Struct. 2008;86:145-63.
[86] Cotsovos D, Pavlović M. Numerical investigation of concrete subjected to compressive impact loading. Part 2: Parametric investigation of factors affecting behaviour at high loading rates. Comput Struct. 2008;86:164-80.
[87] Ross CA, Jerome DM, Tedesco JW, Hughes ML. Moisture and strain rate effects on concrete strength. J Mater. 1996;93:293-300.
[88] Santana HA, Júnior NSA, Ribeiro DV, Cilla MS, Dias CM. 3D printed mesh reinforced geopolymer: Notched prism bending. Cem Concr Compos. 2021;116:103892.
[89] Liu F, Chen G, Li L, Guo Y. Study of impact performance of rubber reinforced concrete. Constr Build Mater. 2012;36:604-16.
[90] Feng W, Liu F, Yang F, Li L, Jing L. Experimental study on dynamic split tensile properties of rubber concrete. Constr Build Mater. 2018;165:675-87.
[91] Chen M, Wang Y, Zhang T, Zhang M. Behaviour of structural engineered cementitious composites under dynamic tensile loading and elevated temperatures. Eng Struct. 2023;280:115739.